



Decoupled phononic-electronic transport in multi-phase *n*-type half-Heusler nanocomposites enabling efficient high temperature power generation

Han Byul Kang^{1,2,*}, Bed Poudel³, Wenjie Li³, Heonjoong Lee^{1,4},
 Udara Saparamadu³, Amin Nozariasbmarz³, Min Gyu Kang³, Adbhut Gupta⁵,
 Jean J. Heremans⁵, Shashank Priya^{1,3,4,*†}

¹ Center for Energy Harvesting Materials and Systems (CEHMS), Virginia Polytechnic Institute and State University, Blacksburg, VA 24061, USA

² Department of Materials Science and Engineering, Virginia Polytechnic Institute and State University, Blacksburg, VA 24061, USA

³ Department of Materials Science and Engineering, Pennsylvania State University, State College, PA 16802, USA

⁴ Department of Mechanical Engineering, Virginia Polytechnic Institute and State University, Blacksburg, VA 24061, USA

⁵ Department of Physics, Virginia Polytechnic Institute and State University, Blacksburg, VA 24061, USA

Strongly coupled electronic and thermal transport behavior in thermoelectric (TE) materials has limited their figure of merit (zT). Here we provide breakthrough in decoupling TE parameters in *n*-type (Hf_{0.6}Zr_{0.4})NiSn_{0.99}Sb_{0.01} half-Heusler (hH) alloys through multi-scale nanocomposite architecture comprising of tungsten nano-inclusions. The tungsten nanoparticles not only assist electron injection, thereby improving electrical conductivity, but also enhance the Seebeck coefficient through energy filtering effect. The microstructure comprises of disordered phases with varying size of microstructural features, which assists in effective scattering of heat-carrying phonons over diverse mean-free-path ranges. Cumulatively, these effects are shown to result in outstanding thermoelectric performance of $zT_{\max} \sim 1.4$ at 773 K and $zT_{\text{avg}} \sim 0.93$ between 300 and 973 K. Using this material, a TE generator is demonstrated, which exhibits high power density of 13.93 W cm⁻² and conversion efficiency of 10.7% under $\Delta T = 674$ K. The fundamental material design principle for TE nanocomposites demonstrated here can be generalized and extended to other TE systems.

Introduction

A rapid increase in global energy demand and greenhouse-gas emissions has turned the spotlight on energy efficiency and waste energy recovery. It is well-known [1–3] that a substantial portion (20–50%) of the energy is lost as waste heat, resulting in total loss of 5–13 quadrillion Btu/yr [4] across US industry. According to Forman's estimation, the fraction of work potential (Carnot potential) for global heat lost with hot-side temperature above 100 °C is 79% and more than 55% waste heat has medium to high hot-side temperature of >300 °C [5]. The Carnot

efficiency of the system (theoretical maximum for converting thermal energy into useful work) increases with hot-side temperature. This indicates the importance of developing waste heat recovery mechanisms that can operate over wide temperature ranges and provide easy integration with variety of industrial processes. In this respect, thermoelectric (TE) energy harvesting is promising as it can provide wide temperature operation through cascading. Further TE modules provide solid-state noiseless operation which is relevant for generator applications.

Half-Heusler (hH) compounds are an important class of TE materials for moderate to high temperature applications due to their excellent mechanical strength and in-air thermal stability [6]. In particular, hH alloys have potential for mass-scale thermoelectric power generation where not only high output power

* Corresponding authors.

E-mail addresses: Kang, H.B. (hbkang@vt.edu), Priya, S. (sup103@psu.edu).

† Shashank Priya is currently at Department of Materials Science and Engineering, Pennsylvania State University, State College, PA 16802, USA.

density but also high mechanical stability and sustainability under repetitive thermal cycling is required. Most widely studied *n*-type MNiSn and *p*-type MCoSb (M = Hf, Zr, and Ti) alloys show much higher hardness (~10 and ~13 GPa) and elastic modulus (~190 and ~220 GPa) compared to that of other TE materials [7,8]. Further, a relatively small difference of coefficient of thermal expansion (CTE) between *n*- and *p*-type hH is beneficial towards long-term durability of TE modules [8]. The commonly used hH alloys exhibit excellent electrical transport properties as a result of sharp slope of the density of states (DOS) near the Fermi level and the narrow band gap (0.1–1.1 eV) [9,10]. However, relatively high thermal conductivity ($7\text{--}17\text{ W m}^{-1}\text{ K}^{-1}$ at 300 K) [11] of hH alloys limits their TE figure-of-merit (zT), defined as $zT = (S^2\sigma/\kappa)T$, where S , σ , and κ are the Seebeck coefficient, electrical conductivity, and thermal conductivity, respectively. The magnitude of thermal conductivity is related to electronic and lattice transport. Various strategies have been developed to effectively reduce the lattice thermal conductivity, such as introducing alloy scattering with additional mass or strain fluctuation [12–14] and enhancing phonon scattering by nanostructuring [15–18].

One promising approach towards suppressing lattice thermal conductivity is through incorporation of nanoscale inclusions into TE materials that enhances phonon scattering. Interestingly, it has been demonstrated that the new interface creation by nanoinclusions simultaneously contributes to improved power factor ($S^2\sigma$) and decreased lattice thermal conductivity through energy filtering. Faleev et al. [19] and Zebardaji et al. [20,21] predicted that a metal–semiconductor interface can provide an adequate potential barrier which can selectively block electrons depending on their energy, resulting in a higher Seebeck coefficient for a given carrier concentration. This effect has been experimentally demonstrated in many TE material systems. Heremans et al. [22] reported that Pb precipitates in PbTe compounds provide thermopower (S) enhancement by increasing the energy dependence of the relaxation time. Sumithra et al. [23] have demonstrated simultaneous reduction in the lattice thermal conductivity and enhancement in power factor by incorporating Bi nanoparticles in the Bi_2Te_3 matrix. Although the effect of nanoinclusions has been demonstrated in hH system, the reported figure of merit for the nanocomposites was much lower than that of unmodified hH compounds ($zT \sim 1$) [24–27]. Makongo et al. [24] revealed large increases in both electrical conductivity and Seebeck coefficient and moderate reduction of thermal conductivity by developing coherent internal phase boundaries in *n*-type full-Heusler/half-Heusler nanocomposites. In this case, the maximum zT of the best nanocomposite was ~ 0.7 at 775 K. Xie et al. [26] have shown similar effects through InSb nanoinclusions and reported that *n*-type (Ti,Zr,Hf)(CoNi)Sb nanocomposites exhibit maximum zT of ~ 0.5 at 820 K. The nanocomposite strategies for hH system work on certain level, but overall they are not effective as much as in other TE materials. This is due to poor TE performance of base hH matrix and compatibility and stability problem of inclusions within hH alloys at high temperatures.

In this study, we demonstrate simultaneous multi-scale phonon scattering and energy filtering of hot electrons in *n*-type $(\text{Hf}_{0.6}\text{Zr}_{0.4})\text{NiSn}_{0.99}\text{Sb}_{0.01}$ nanocomposites through introduction

of tungsten nanoinclusions and nanoprecipitation. High melting point of the tungsten assists in suppressing undesirable reaction with hH matrix and grain growth at high synthesis temperatures. Our results show that the tungsten nanoparticles play a key role in effectively decreasing the thermal conductivity of the composite by boosting phonon scattering that is attributed to both interfacial phonon scattering between hH and tungsten due to large difference in acoustic impedance and integrated phonon scattering at broad length scale by forming multi-scale nanostructure. In addition, the tungsten nanoinclusions simultaneously enhance the electrical conductivity and Seebeck coefficient by creating a potential barrier at the metal/semiconductor interface, which creates an electron energy filtering effect. Owing to these favorable changes in electrical and thermal properties, we achieved a noticeably high figure of merit ($zT_{\text{max}} \sim 1.37$ at 873 K and $zT_{\text{avg}} \sim 0.91$ in the range from 300 K to 973 K) for the optimum level of tungsten concentration of 5 wt% in *n*-hH/W nanocomposites. Further, using this nanocomposite material we demonstrate an outstanding TE device with power density of 13.93 W cm^{-2} and conversion efficiency of 10.7% across 674 K temperature gradient.

Results and discussion

Multiple phase nanocomposites through tungsten inclusions

Fig. 1a illustrates the multi-scale structure in *n*-type hH nanocomposite with tungsten inclusions and nanoprecipitates. First, we designed the pristine hH matrix to optimize TE performance through compositional tuning and combination of RF inductive melting and spark plasma sintering. At the atomic level, multicomponent alloying of Hf and Zr at *M* sites facilitates lower thermal conductivity by strong phonon scattering at point defects in the lattice [31]. In addition, the rapid fabrication process introduces nano-sized hafnium precipitates in the hH matrix, which contributes towards improvement of TE performance [32,33]. The pristine *n*-type hH compound exhibits comparable TE performance with the state-of-art zT as shown in Fig. 1b [17,28–30]. Next, metallic nanoparticles are incorporated in the base hH matrix as depicted in Fig. 1a. Several parameters were considered in determining the inclusion material: (i) stability and compatibility with the matrix at elevated temperatures, (ii) large acoustic impedance mismatch between a metal (inclusions) and a semiconductor (TE materials), which is beneficial for increasing the phonon scattering effect at the metal–semiconductor interface, (iii) low heat capacity, and (iv) a multi-length scale architectural design with the nanoprecipitates, which efficiently scatters heat-carrying phonons. Tungsten nanoparticles were found to meet all these criteria and thus were selected as an inclusion material. The tungsten inclusions play important role in not only reducing thermal conductivity but also enhancing electronic transport properties. The best composition for the tungsten/hH nanocomposite shows record high figure of merit in the overall temperature region up to 973 K (Fig. 1b).

The desired phase formation for $(\text{Hf}_{0.6}\text{Zr}_{0.4})\text{NiSn}_{0.99}\text{Sb}_{0.01} + x$ wt% tungsten (W) nanocomposites ($x = 0, 2, 5, \text{ and } 10$) was confirmed from X-ray diffraction analysis (Supplementary Fig. S1). All samples exhibited half-Heusler phase without any secondary phases. Tungsten phase (JC-PDS, 00-004-0806) was observed in

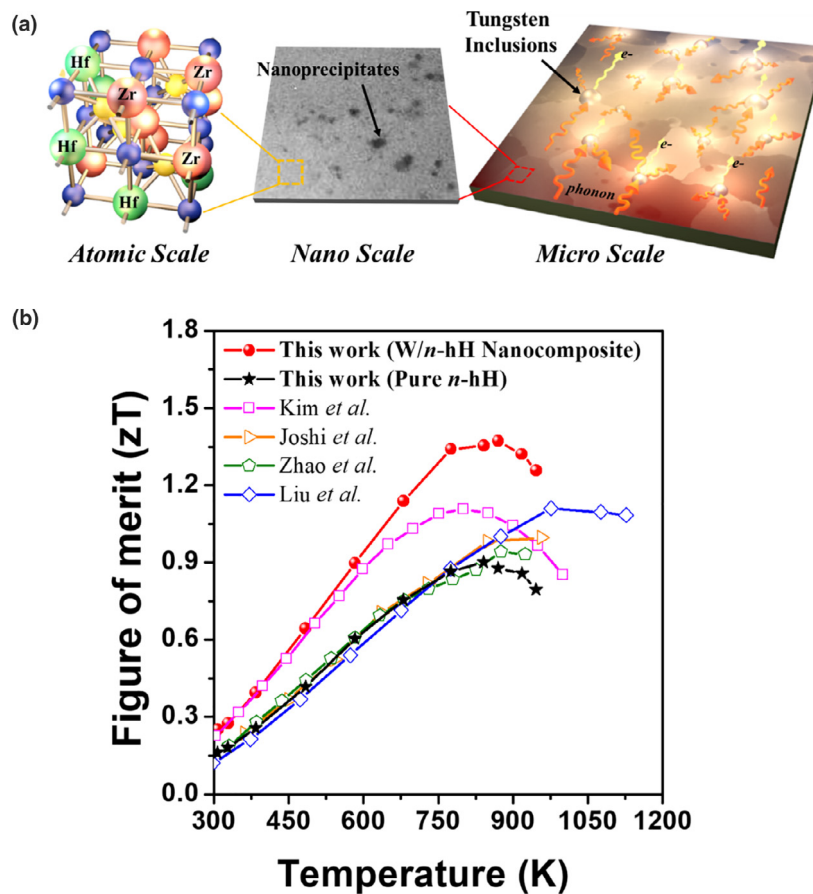


FIGURE 1

Schematic illustration of the nanocomposite and figure of merit comparison. (a) The structure of multi-scale *n*-type hH nanocomposite with tungsten inclusions. (b) The comparison of thermoelectric performance of the pure *n*-hH and the nanocomposites developed in this work with other literatures [17,28–30].

the diffraction patterns and the intensity of tungsten peaks increased at higher concentration of tungsten nanoparticles. We verified the distribution of tungsten nanoparticles by scanning electron microscopy (Supplementary Fig. S2). The backscattered electron diffraction (BSED) image and corresponding energy-dispersive X-ray spectroscopy (EDS) demonstrated that tungsten nanoparticles are homogeneously and widely dispersed in the hH matrix. Tungsten has a high melting point (3422 °C) which restricts grain growth of tungsten nanoparticles even under high sintering temperature of 1150 °C. This advantage provides stable distribution of nano-inclusions in the hH matrix as represented in EDS mapping. The grain size is not dependent on the concentration of tungsten inclusions and the average grain size of the hH matrix is 1.39 μm.

To probe the nanoscale distribution of tungsten inclusions in the hH matrix, we have performed transmission electron microscopy on a representative sample of (Hf_{0.6}Zr_{0.4})NiSn_{0.99}Sb_{0.01} + 5 wt% W nanocomposite as shown in Fig. 2. The inclusions are mostly located at the vicinity of the grain boundary, which is the preferred site for the precipitation of new phase. The microscopic EDS mapping clearly demonstrates distribution of tungsten nanoparticles in hH matrix (Fig. 2b and c). The pristine hH matrix has an intrinsic hafnium and hafnium oxide (HfO₂) precipitates resulting from a supersaturation of high melt-

ing point of hafnium during rapid cooling process (Supplementary Fig. S3). The EDS mapping of pure hH sample in Fig. S3 reveals that the nano-sized precipitates (~20 nm) are widely dispersed within the grain and at the grain boundary. It has been reported that the nano-scale Hf-phase precipitates and phase separation are spontaneously induced in the *n*-type hH compounds under rapid cooling/heating condition. A small concentration of oxygen absorbed on the surface of precursors and partial solubility of hafnium in the alloys due to high melting point of the hafnium results in the formation of hafnium and hafnium oxide precipitates during the cooling process [32–35]. The nanoscale hafnium and HfO₂ precipitates were also observed around the tungsten nano-inclusions (green dots) in the TEM images. The size of Hf-phase is in the range of tens of nanometer as shown in Fig. 2c (green circles). The dimension of the tungsten inclusions is observed in the range from 30 nm to 274 nm and the average inclusion size is found to be 98 nm (Inset of Fig. 2c). The size of Hf-phase precipitates is much smaller than the tungsten inclusions, and the average value is found to be 18 nm. Consequently, we found that the tungsten/*n*-hH nanocomposite comprises of multiple phases with dimensions ranging from tens of nanometer (hafnium/HfO₂) to several hundreds of nanometer (tungsten). This results in enhanced phonon scattering and thereby lower thermal conductivity [36].

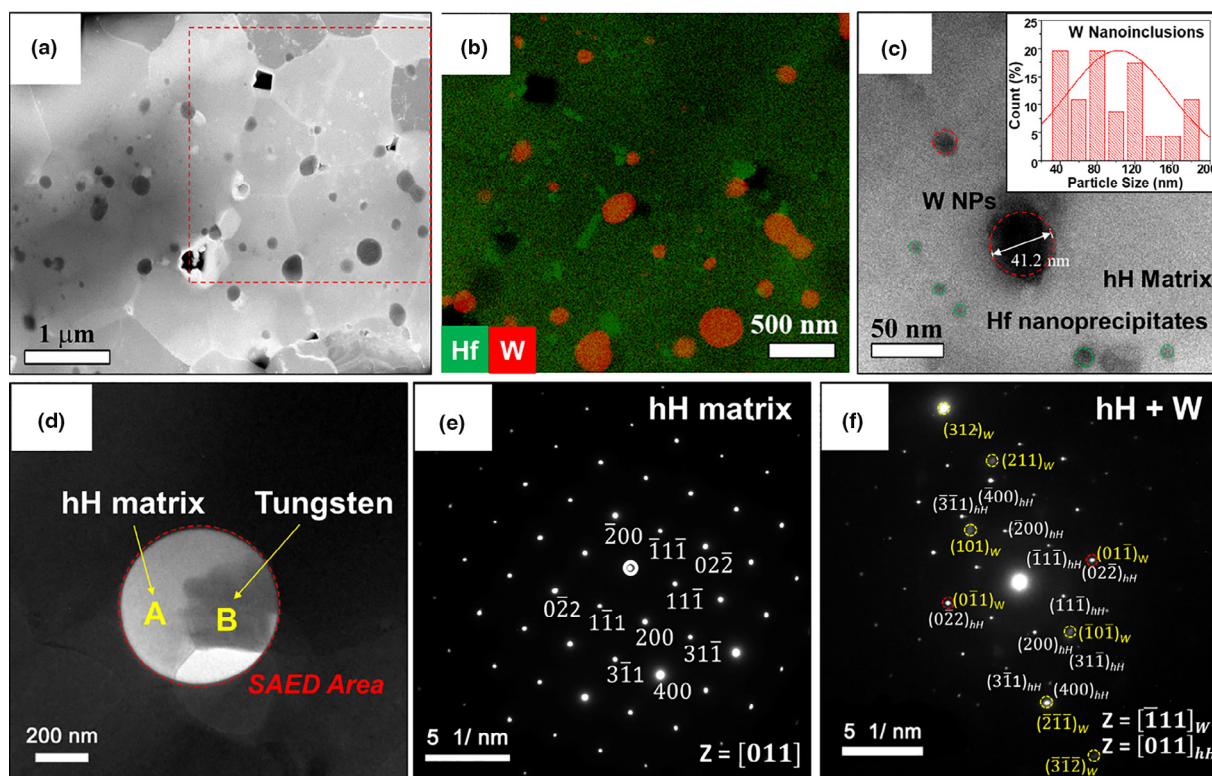


FIGURE 2

Structural characterizations of the hH/tungsten (W) nanocomposites. (a) Transmission electron micrograph (TEM) of $(\text{Hf}_{0.6}\text{Zr}_{0.4})\text{NiSn}_{0.99}\text{Sb}_{0.01} + 5 \text{ wt\% W}$ nanocomposite. (b) Elemental mapping on the selective area. Red color indicates a tungsten element and green color shows a hafnium element. (c) Enlarged TEM image of the tungsten nanoparticles and histogram of tungsten particle size distribution (inset). (d) The spot of selective area electron diffraction (SAED) for n -hH + 5 wt% W nanocomposite. (e) and (f) SAED patterns of the region A (hH matrix, e), and the region B, respectively (hH matrix and tungsten, f).

The interfacial relationship between hH matrix and tungsten inclusion was investigated using selective area electron diffraction (SAED) as shown in Fig. 2d. We selected two regions that are associated with the pure hH matrix and tungsten nano-inclusions for structural analysis using EDS (marked as A and B in Fig. 2d). The SAED patterns from each region are shown in Fig. 2e and f, respectively. The hH matrix shows face-centered cubic diffraction pattern (Fig. 2e) and additional diffraction spots with body-centered cubic symmetry corresponding to tungsten inclusion (Fig. 2f), which are marked as yellow circle. The $(\text{Hf}_{0.6}\text{Zr}_{0.4})\text{NiSn}_{0.99}\text{Sb}_{0.01}$ half-Heusler alloy has a space group of $F\bar{4}3m$ with a lattice constant of 6.077 Å. Tungsten has a space group of $\text{Im}\bar{3}m$ with a lattice constant of 3.165 Å. Thus, the new phase tends to form a partially coherent interface with matrix with a specific crystallographic orientation relationship that minimizes misfit energy of the system. For half-Heusler (*fcc* structure), there are three close-packed planes, $(111)_{\text{hH}}$, $(200)_{\text{hH}}$, and $(220)_{\text{hH}}$. The close-packed planes for tungsten (*bcc*

structure) are $(110)_{\text{W}}$, $(200)_{\text{W}}$, and $(211)_{\text{W}}$, opening nine possibilities for presence of matching interface between hH and tungsten [37]. The d -value mismatch ($\delta = (d_{\beta} - d_{\alpha})/d_{\alpha}$) between the nine possible plane pairs are listed in Table 1. The pair corresponding to $(220)_{\text{hH}}$ and $(110)_{\text{W}}$ plane shows the smallest mismatch of -3.67% and the d -value mismatch in all the other plane pairs is greater than a critical mismatch of 6% [37]. The SAED pattern reveals the matching along $(0\bar{1}1)_{\text{W}}$ and $(022)_{\text{hH}}$ planes marked as red circle in Fig. 2f. This indicates that tungsten inclusions are incorporated in the hH matrix with a semi-coherent interface that results in lowering of the Gibbs energy.

Outstanding improvement in PF with electron injection and energy filtering effect

The temperature dependence of electronic transport properties of all the nanocomposites are shown in Fig. 3. The electrical conductivity of hH alloy varied as a function of tungsten concentration. It gradually increased from $1.18 \times 10^5 \text{ S}\cdot\text{m}^{-1}$ for n -hH to

TABLE 1

d -Value mismatch (%) along possible matching planes between half-Heusler and tungsten.

Matching plane	d -Value mismatch (%)	Matching plane	d -Value mismatch (%)	Matching plane	d -Value mismatch (%)
$(111)_{\text{hH}}/(110)_{\text{W}}$	57.1	$(200)_{\text{hH}}/(110)_{\text{W}}$	36.1	$(220)_{\text{hH}}/(110)_{\text{W}}$	-3.67
$(111)_{\text{hH}}/(200)_{\text{W}}$	122.0	$(200)_{\text{hH}}/(200)_{\text{W}}$	92.3	$(220)_{\text{hH}}/(200)_{\text{W}}$	36.1
$(111)_{\text{hH}}/(211)_{\text{W}}$	171.8	$(200)_{\text{hH}}/(211)_{\text{W}}$	135.5	$(220)_{\text{hH}}/(211)_{\text{W}}$	66.7

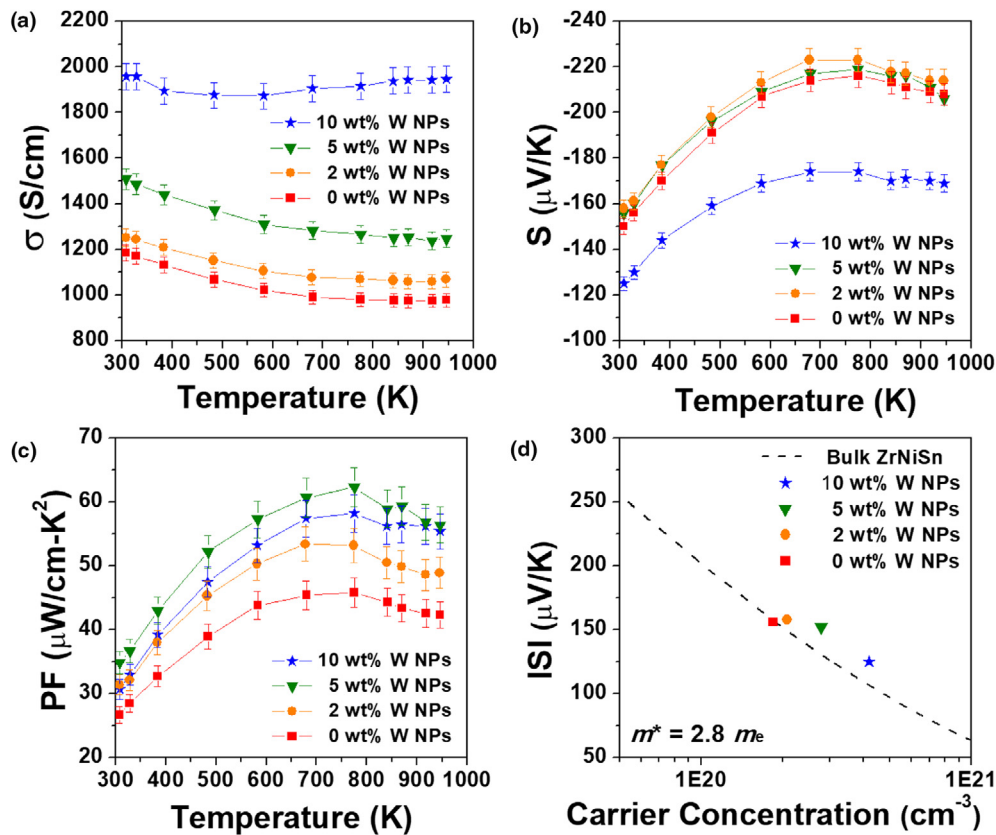


FIGURE 3

Electronic transport properties of hH/W nanocomposites. (a) Temperature dependence of electrical conductivity. (b) Seebeck coefficient, and (c) power factor as a function of tungsten concentration, respectively. (d) Carrier concentration dependence of Seebeck coefficient at room temperature.

$1.51 \times 10^5 \text{ S m}^{-1}$ for *n*-hH/5 wt% W composites and reached to $1.96 \times 10^5 \text{ S m}^{-1}$ for *n*-hH/10 wt% W composite at 300 K, resulting in 65% enhancement. This enhancement is caused by the increase in carrier concentration due to the presence of metallic tungsten nanoparticles. It has been demonstrated that metallic nanoparticle inclusions can be more effective in adding electrons to the conduction band in *n*-type semiconductor compared to dopants [23]. Table 2 shows that the carrier concentration and mobility vary with tungsten inclusions. The Hall resistivity used to obtain the data in Table 2 also indicates single-carrier electronic conduction. The carrier concentration almost doubles with 10 wt% tungsten inclusion compared to pure *n*-hH. This provides evidence of the electron injection from metallic tungsten nanoparticles into the semiconductor hH matrix, resulting in increased electrical conductivity. Interestingly, only minor

changes are observed in the Seebeck coefficient with relatively low concentration of tungsten inclusions of 2 and 5 wt%. On the contrary a large drop is present at a high concentration of 10 wt% tungsten inclusion as represented in Fig. 3b. The Seebeck coefficient can be defined by Mott formula as [38,39]:

$$S = \frac{\pi^2}{3} \frac{k_B}{q} k_B T \left\{ \frac{1}{n} \frac{dn(E)}{dE} + \frac{1}{\mu} \frac{d\mu(E)}{dE} \right\}_{E=E_F} \quad (1)$$

where k_B is Boltzmann's constant, q is the carrier charge, E_F is the Fermi energy, $n(E)$ and $\mu(E)$ are the density and mobility of carrier at energy E , respectively. From the Eq. (1), the Seebeck coefficient depends on the energy derivative of carrier density and mobility. It indicates that higher Seebeck coefficient can be achieved by both a sharp modulation in the carrier density of states (DOS) near E_F (increase in $dn(E)/dE$) and the energy filtering effect that selectively scatters low energy charge carriers (higher $d\mu(E)/dE$) [6,39]. Fig. 3d shows the carrier concentration dependence of the Seebeck coefficient at room temperature. The dashed line represents the calculated Seebeck coefficient of bulk ZrNiSn alloy, derived from the a single Kane band (SKB) model with the DOS effective mass $m^* = 2.8 m_e$ [12]. Our *n*-type hH alloy shows good agreement with the calculated value on the dashed line. It is noteworthy that the introduction of nano inclusions in hH matrix results in deviation from the calculated bulk ZrNiSn values, showing higher Seebeck coefficient at a given carrier concentration. This provides strong evidence of the energy filtering effect that results in enhanced Seebeck coefficient by increasing $d\mu(E)/dE$ in

TABLE 2

Carrier (electron) concentration and mobility of $(\text{Hf}_{0.6}\text{Zr}_{0.4})\text{NiSn}_{0.99-\text{Sb}_{0.01}} + x \text{ wt\% W}$ nanocomposites at room temperature, deduced from magnetotransport (Hall effect) measurements.

Samples	S (μV/K)	Carrier concentration ($\times 10^{19} \text{ cm}^{-3}$)	Carrier mobility ($\text{cm}^2 \text{ V}^{-1} \text{ s}^{-1}$)
$x = 0 \text{ wt\%}$	-156	18.52	40.60
$x = 2 \text{ wt\%}$	-158	20.79	36.70
$x = 5 \text{ wt\%}$	-152	27.85	28.87
$x = 10 \text{ wt\%}$	-125	41.82	26.83

the Eq. (1). The power factor ($S^2\sigma$) was significantly enhanced by introducing tungsten nano-inclusions into the hH matrix (Fig. 3c). The maximum power factor reached $62.3 \mu\text{W}\cdot\text{cm}^{-1}\cdot\text{K}^{-1}$ at 773 K for 5 wt% W/n-hH nanocomposite, which is a 36% improvement compared to pure n-hH. It is attributed to both an increase of the electrical conductivity by charge carrier injection from metallic tungsten nano-inclusions, and the relatively higher Seebeck coefficient at the given carrier concentration by energy filtering effect.

Thermal conductivity reduction in n-hH/W nanocomposite

The thermal conductivity (κ) of the nanocomposite was calculated from the measured density (ρ), specific heat capacity (C_p), and thermal diffusivity using equation $\kappa = \rho C_p \alpha$. As shown in Fig. 4a, the specific heat capacity of the nanocomposites decreases on increasing tungsten concentration, due to the contribution of lower specific heat capacity of tungsten ($0.132 \text{ J}\cdot\text{g}^{-1}\cdot\text{K}^{-1}$). In the case of an isotropic composite with no local stress or strain, the specific heat capacity of the composite can be expressed using mixing rule:

$$C_p = x_1 C_{p1} + x_2 C_{p2} + \dots + x_n C_{pn} = \sum x_k C_{pk} \quad (2)$$

where $x_k = m_k/m$ is mass fraction, and C_{pk} is a specific heat capacity of component k . The calculated C_p values for each sample of n-hH/W nanocomposites are illustrated as dotted line in Fig. 4a. The measured specific heat capacity shows a good correlation according to Eq. (2) except in the lower temperature region. Thus, the intrinsic low specific heat capacity of tungsten can contribute

towards decrement of thermal conductivity of the composite, independent of the scattering effect of the inclusions. The total thermal conductivity of n-hH/W nanocomposites was effectively reduced by adding tungsten nanoparticles as shown in Fig. 4b. It should be noted that high concentration of tungsten inclusions is not beneficial in decreasing thermal conductivity because a large contribution of electronic thermal conductivity arising from higher carrier concentration offsets the effect of enhanced phonon scattering by nano-inclusions. To clarify the influence of nano-inclusions on the thermal transport by phonon scattering, we derived lattice thermal conductivity (κ_{lat}) by subtracting the electronic component κ_e from the total thermal conductivity κ_{tot} ($\kappa_{lat} = \kappa_e - \kappa_{tot}$). The electronic contribution (κ_e) can be estimated by Wiedemann–Franz law:

$$\kappa_e = L\sigma T \quad (3)$$

where L is the Lorenz number calculated by a single Kane band (SKB) model incorporating multiple scattering mechanisms of ZrNiSn based hH alloys [12,40]. The electronic contribution of the thermal conductivity becomes comparable with the lattice thermal conductivity when the tungsten fraction is sufficiently high (Supplementary Fig. S4). Fig. 4c presents the temperature dependence of the lattice thermal conductivity of n-hH/W nanocomposites. The lattice thermal conductivity was effectively suppressed by the addition of tungsten nanoparticles. Higher concentrations of tungsten inclusions showed lower lattice thermal conductivity, indicating the increase of phonon scattering. For

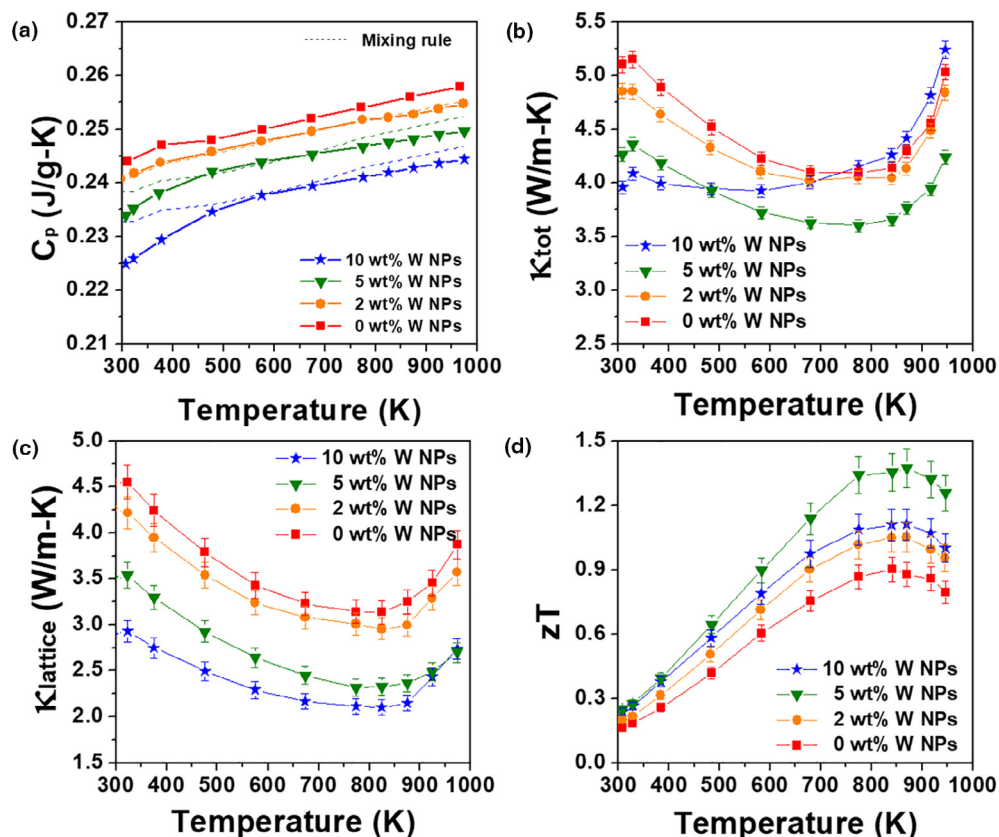


FIGURE 4

Thermal transport properties of hH/W nanocomposites. (a) Temperature dependence of specific heat capacity, (b) total thermal conductivity, (c) Lattice thermal conductivity ($\kappa_{lattice}$) derived by subtracting an electronic component (κ_e) from the κ_{tot} , and (d) figure of merit zT , respectively.

example, a room temperature value of $\kappa_{\text{lat}} \approx 4.55 \text{ W}\cdot\text{m}^{-1}\cdot\text{K}^{-1}$ was greatly decreased to $2.93 \text{ W}\cdot\text{m}^{-1}\cdot\text{K}^{-1}$ in the 10 wt% tungsten inclusion sample, a change of 35%. The reduction of lattice thermal conductivity via tungsten inclusions was observed over a wide temperature range. Next, we discuss mechanisms that contribute to the lower lattice thermal conductivity in the presence of tungsten inclusions.

A large acoustic impedance mismatch between a semiconductor and a metal leads to a high effective interface phonon scattering [41]. The acoustic impedance (Z) of a material is defined as the product of the density (ρ) and the speed (c) of the sound waves traveling in the medium:

$$Z = \rho c \quad (4)$$

Since the half-Heusler semiconductor matrix and the tungsten metal particles have a significant difference in both the density ($\rho_{\text{hH}} = 9.37 \text{ g}\cdot\text{cm}^{-3}$ and $\rho_{\text{W}} = 19.3 \text{ g}\cdot\text{cm}^{-3}$) and the speed of sound ($c_{\text{hH}} [42] = 3367 \text{ m}\cdot\text{s}^{-1}$, and $c_{\text{W}} = 5174 \text{ m}\cdot\text{s}^{-1}$), there is a large acoustic impedance mismatch between $Z_{\text{hH}} = 3.16 \times 10^7 \text{ kg}\cdot\text{m}^{-2}\cdot\text{s}^{-1}$ and $Z_{\text{W}} = 9.99 \times 10^7 \text{ kg}\cdot\text{m}^{-2}\cdot\text{s}^{-1}$. However, hafnium shows similar acoustic impedance ($Z_{\text{Hf}} = 4.01 \times 10^7 \text{ kg}\cdot\text{m}^{-2}\cdot\text{s}^{-1}$) as that of half-Heusler matrix. Further, hafnium oxide has relatively small difference in acoustic impedance ($Z_{\text{HfO}_2} = 5.23 \times 10^7 \text{ kg}\cdot\text{m}^{-2}\cdot\text{s}^{-1}$) as shown in Table 3. This indicates that the interfacial phonon scattering can be more predominant for tungsten inclusions rather than hafnium or hafnium oxide, and thus the lattice thermal conductivity is substantially decreased by increasing the interfaces with tungsten.

A multiphase nanostructure with varying length-scales was developed through mixture of hafnium/HfO₂ precipitates, tungsten inclusions, and mesoscale grains of hH matrix. This type of microstructure can further contribute to an additional reduction in lattice thermal conductivity by inducing integrated phonon scattering across multiple length scales. For example, phonons with short and medium mean free paths of less than 100 nm can be scattered by both hafnium/HfO₂ precipitates and tungsten inclusions. Mesoscale grain structure can contribute to scattering of heat-carrying phonons with longer mean free path. Biswas et al. [36] have shown that phonon scattering is more effective by designing hierarchical architectures in *p*-type PbTe-SrTe doped with 2 mol% sodium. Zhang et al. [43] have also reported outstanding TE performance in *n*-type PbTe by inducing a multiphase nanostructure via In, Sb, Pb, and InSb nanoprecipitates. These prior results match our findings and confirm the effectiveness of multiphase multi-length microstructures.

TABLE 3

Comparison of the acoustic impedance in three mediums of (Hf_{0.6}Zr_{0.4})NiSn_{0.99}Sb_{0.01} (*n*-hH), hafnium, hafnium oxide (HfO₂) and tungsten according to their density and speed of sound.

Materials	Density (g/cm ³)	Speed of sound (m/s)	Acoustic impedance (10 ⁷ kg/m ² s)
<i>n</i> -hH	9.37	3367	3.16
Hafnium	13.31	3010	4.01
HfO ₂	9.68	5405	5.23
Tungsten	19.3	5174	9.99

High power density TEG based on nanocomposite

Simultaneous improvement in the power factor and reduction in thermal conductivity boost the figure of merit (zT) in entire temperature region, as represented in Fig. 4d. The maximum zT value reached to ~ 1.4 at 873 K with 5 wt% tungsten inclusion into the *n*-type hH matrix, 55% improvement compared to hH sample ($zT_{\text{max}} \sim 0.9$ at 823 K). More importantly, the results show that the zT value is improved over a broad temperature range from 300 K to 973 K. The average zT in the temperature range of 573 K to 973 K increases from ~ 0.78 to ~ 1.20 through incorporation of 5 wt% tungsten inclusions. As shown in Fig. 1b, this is a remarkable improvement compared to current state-of-art *n*-type hH alloys, such as the Ti_{0.5}Hf_{0.5}NiSn_{0.98}Sb_{0.02} alloy with atomic-scale defect disorders ($zT = 1.09 \pm 0.12$ at 800 K) [28], the Hf and Nb alloying in (Hf_{0.25}Zr_{0.75})NiSn_{0.99}Sb_{0.01} and (Zr_{0.4}-Hf_{0.6})_{0.88}Nb_{0.12}CoSb compounds with zT of ~ 1.0 at 1000 K [29,31], and nanostructured (Hf_{0.75}Zr_{0.25})NiSn_{0.99}Sb_{0.01} compounds ($zT \sim 1.0$ at 873 K) [17]. The reproducibility of the TE performance for the nanocomposite is confirmed using nanocomposite samples synthesized in separate batches (See the Supplementary Fig. S5). It is noteworthy that the zT improvement in our multi-phase nanocomposites is attributed to a supplementary advantage of tungsten nano-inclusion in addition to the various strategies demonstrated for the hH alloys. This implies that the multi-scale nanocomposite technique demonstrated here can be extended to other TE materials that have been optimized by atomic and nanoscale modifications to further enhance their performance.

To further demonstrate the significant improvement of TE performance in the *n*-hH/W nanocomposite material, we developed a half-Heusler based uni-couple TEG device using the *n*-type nanocomposite hH and *p*-type (Hf_{0.5}Zr_{0.5})CoSb_{0.8}Sn_{0.2} hH material. The selected *p*-type material has very similar coefficient of linear thermal expansion (CTE) as that of our *n*-type hH composition and high figure of merit zT (See the Supplementary Fig. S6). In order to effectively translate the TE materials performance to the device, it is essential to minimize the parasitic losses due to the contact resistance between the TEG legs and electrodes [44]. The effective ZT of the thermoelectric device is given by the following equation [45,46],

$$(ZT)_D = \frac{l}{l + 2\sigma r_c} (ZT)_M \quad (5)$$

where l is the length of the thermoelectric leg, r_c is the contact resistance, σ is the electrical conductivity and $(ZT)_M$ is the effective ZT of the thermoelectric material between the hot-side and the cold-side. The electrical conductivity for (Hf,Zr)NiSn based materials is about $\sim 10^5 \text{ S}\cdot\text{m}^{-1}$ at room temperature, which means a very low r_c plays a prominent role in controlling the TE device performance according to Eq. (5). For power generation applications, *p*-type and *n*-type materials are connected in series by brazing onto a conductive substrate. The brazing material should have high electrical and thermal conductivity, possess similar thermal expansion as that of TE material, exhibit high wetting capability with the material surface and avoid interfacial reactions [46]. Here, we connected the thermoelectric legs with the copper interconnect high-temperature brazing material. The contact resistance (r_c) of *p*- and *n*-type legs with the brazing material were

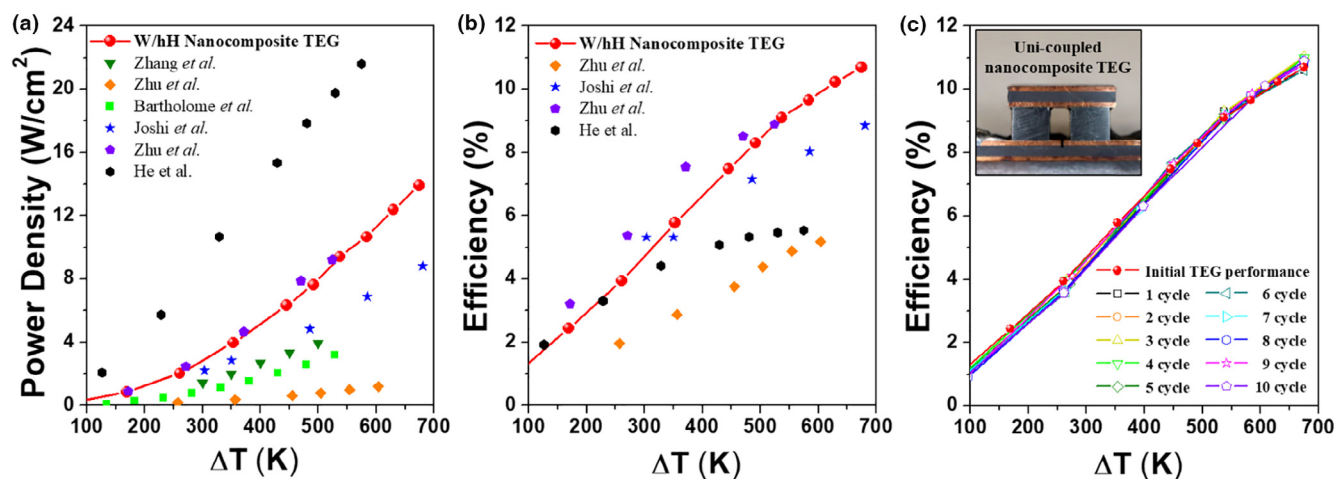


FIGURE 5

Thermoelectric generator (TEG) performance of the nanocomposite. Comparison of (a) power density, (b) conversion efficiency of the nanocomposite TEG developed in this work and other half-Heusler based TEGs [47–52] reported in previous studies as a function of temperature difference (ΔT), and (c) reliability test on the TEG device after thermal cycling between 373 K and 1023 K for a given number of cycles.

measured to be $\sim 2 \mu\Omega\text{-cm}^2$ and $\sim 1 \mu\Omega\text{-cm}^2$ respectively, showing exceptionally low values. The test set up for the measurement of the thermoelectric output power and efficiency is illustrated in [Supplementary Fig. S7](#). Internal resistance (r_i), short circuit current (I_{SC}), and peak output power (P_{max}) for the device can be evaluated using the expressions:

$$r_i = \frac{V_{oc} - V_d}{I_d} \quad (6)$$

$$I_{SC} = \frac{V_{oc}}{2r_i} \quad (7)$$

$$P_{max} = \frac{V_{oc}^2}{4r_i} \quad (8)$$

where, V_d is the device voltage and I_d is the device current.

We measured the open circuit voltage (V_{oc}), device voltage (V_d), calculated the internal resistance (r_i) and determined the peak power output (P_{max}) by varying hot-side temperature from 473 K to 1023 K under nearly constant cold-side temperature of 293 K. At temperature difference (ΔT) of 674 K, the uni-couple TEG showed $V_{oc} \sim 230.31$ mV, $I_{SC} \sim 12.25$ A and the $P_{max} \sim 1410.7$ mW. The uni-couple resistance (r_i) is ~ 9.4 m Ω at the highest temperature. The temperature dependence of output voltage (V_{oc}) and maximum peak power (P_{max}) is shown in [Supplementary Fig. S8](#). The power density of uni-couple hH TEG is calculated from the peak power output and the activation area of TEG as shown in [Fig. 5a](#). The power density of this device was measured to be ~ 13.93 W $\cdot\text{cm}^{-2}$ across a temperature difference of 674 K. [Fig. 5b](#) shows the conversion efficiency of the nanocomposite TEG. The outstanding conversion efficiency of 10.7% was achieved at $\Delta T = 674$ K. We compare results from other hH-based TEGs reported in the literature with our nanocomposite TEG [47–52]. Zhang et al. [50] developed a 1 kW TEG system comprising of 400 TEG modules under a temperature difference of 339 K, where the TEG module produced a power density of 4 W $\cdot\text{cm}^{-2}$ across a temperature difference of 500 K. Zhu et al. [49] demonstrated a power density of

1.2 W $\cdot\text{cm}^{-2}$ under $\Delta T = 603$ K from a hH module based on n -type ZrNiSn alloys and p -type FeNb_{0.8}Ti_{0.2}Sb compounds. Seven pairs of uni-couple hH module were demonstrated by Bartholome et al. [51] that exhibited power density of 3.2 W $\cdot\text{cm}^{-2}$ under $\Delta T = 527$ K. Joshi et al. [48] reported the power density of ~ 8.9 W $\cdot\text{cm}^{-2}$ with a high conversion efficiency of 8.9% across a temperature difference of 678 K. The highest output power in TEG device has been reported by He et al. [52] on the order of 22 W $\cdot\text{cm}^{-2}$ using single leg TEG. The device utilized a high power factor p -type hH compound with formulation Nb_{0.95}Ti_{0.05}-FeSb and operated under the hot-side temperature of 868 K. However, high thermal conductivity of this material led to a relatively low conversion efficiency of 5.6%. Zhu et al. [47] recently demonstrated a good transition of the record high zT into outstanding TEG performances in p -type ZrCoBi_{0.65}Sb_{0.15}Sn_{0.20}. The single leg TEG for ZrCoBi shows the peak power density of ~ 9.3 W $\cdot\text{cm}^{-2}$ and the conversion efficiency of $\sim 9\%$ at the hot-side temperature of 823 K. As represented in [Fig. 5a](#) and [b](#), our TEG compares favorably with the record high TEG performance over a wide temperature range and exhibits remarkable power density of ~ 13.93 W $\cdot\text{cm}^{-2}$ and conversion efficiency of $\sim 10.7\%$ at $\Delta T = 674$ K. In addition, the TEG shows stable and reliable output performance under thermal cycling between 373 K and 1023 K up to 10 times as shown in [Fig. 5c](#) (See the [Supplementary Fig. S8](#) for the repeatability data on output power). This result confirms that the significant improvement obtained in material performance can be translated into excellent TEG device performance through an optimized manufacturing process that results in reduced contact resistance.

Conclusions

We demonstrate high thermoelectric performance of n -type hH alloy through incorporation of tungsten nanoinclusions. A multiphase multi-length-scale microstructure comprising of hafnium/HfO₂ nanoprecipitates, tungsten nanoinclusions, and mesoscale hH grains was found to be highly effective in enhancing the phonon scattering. Reduction in lattice thermal conduc-

tivity was induced by large acoustic impedance mismatch between the tungsten and hH matrix and multiple nanophase architecture. The metallic tungsten injects electrons in to the host hH semiconductor which increases electrical conductivity. Higher Seebeck coefficient was achieved for given carrier concentration by energy filtering effect at the interfaces between metal inclusions and semiconductor matrix. As a result, an outstanding maximum zT of ~ 1.4 at 873 K and average zT of ~ 0.9 in the temperature range of 300–973 K were achieved for hH alloy with 5 wt % tungsten nanoinclusions. The enhancement in material properties were translated in to TEG uni-couple hH module that exhibited high output power density of $13.93 \text{ W}\cdot\text{cm}^{-2}$ and conversion efficiency of 10.7% under a temperature difference of 674 K. These results are encouraging for practical thermoelectric application in waste heat recovery systems.

Methods

Sample synthesis

(Hf_{0.6}Zr_{0.4})NiSn_{0.99}Sb_{0.01} alloys were synthesized using radio-frequency induction melting under an argon atmosphere for 5 min. Stoichiometric amounts of high purity metal precursors of hafnium piece (99.9%, Alfa Aesar), zirconium slug (99.9%, Alfa Aesar), nickel slug (99.995%, Alfa Aesar), antimony shot (99.999%, Alfa Aesar), and tin wire (99.95%, Alfa Aesar) were mixed to obtain the desired composition. The ingots were rotated and remelted several times to ensure homogeneity. The resulting ingots were pulverized and transferred in a stainless steel container with grinding balls under an argon environment in a glove box. Mechanical milling was conducted for 4 hours using SPEX mixer/mill (Model 8000D, SPEX SamplePrep, Metuchen, NJ). Grinded hH powders were mixed in three different amounts ($x = 2, 5,$ and $10 \text{ wt}\%$) with tungsten nanoparticles (99.7%, Sky Spring Nanomaterials) by using SPEX mixer/mill. The size of raw tungsten nanoparticles ranges from 40 to 100 nm in diameter and the average particle size (APS) is 40–60 nm. The mixed powders were consolidated by Spark Plasma Sintering (SPS, Model Dr. Sinter-625V, Fuji, Japan) at 1150 °C under a pressure of 80 MPa for 5 min, yielding fully dense pellets.

X-ray diffraction and microscopy

The crystal structure and phase formation was investigated using high resolution X-ray diffractometer (Model D8 advance, Bruker) with Cu-K α radiation ($\lambda = 1.5418 \text{ \AA}$). The refinement by Rietveld method was applied using PANalytical X'Pert Highscore plus software. The microstructure and elemental distribution of the nanocomposites were studied using environmental scanning electron microscope (ESEM, Quanta 600 FEG, FEI) and high-resolution transmission electron microscope (HRTEM, JEOL 2100, JEOL Ltd., Tokyo, Japan).

Physical property characterization

The electrical conductivity and Seebeck coefficient were simultaneously measured over the temperature range of 300–973 K using a commercial Seebeck coefficient/electric resistance measuring system (ZEM-3, Ulvac-Riko, Japan). The thermal conductivity was determined through the measurement of thermal diffusivity using a laser flash system (TC-1200RH, Ulvac-Riko, Japan). Specific heat (C_p) was measured with a differential scan-

ning calorimeter (DSC 214, Netzsch, Germany). Magnetotransport data, consisting of Hall resistivity (transverse electrical resistivity yielding carrier density) and longitudinal resistivity (yielding electrical conductivity and carrier mobility) were measured in a dedicated magnetotransport setup at room temperature (298 K), using 4-point contact van der Pauw sample configurations with indium-paint ohmic contacts. Data was obtained over magnetic fields up to 1.4 T, with a sample current excitation of 200 mA rms. A voltage preamplifier and lock-in amplifier were used to measure the voltage signals. The linearity of the current–voltage characteristics of the ohmic contacts was verified up to the 200 mA excitation current.

TEG module fabrication

The uni-couple hH based TEG module was fabricated using *n*-type (Hf_{0.5}Zr_{0.5})NiSn_{0.99}Sb_{0.01} half-Heusler with 5 wt% of tungsten nanocomposites and *p*-type (Hf_{0.5}Zr_{0.5})CoSb_{0.8}Sn_{0.2} compounds. The hH wafers were cut into $2.2 \text{ mm} \times 2.2 \text{ mm} \times 1.94 \text{ mm}$ legs for *n*-type and $2.3 \text{ mm} \times 2.3 \text{ mm} \times 1.95 \text{ mm}$ legs for *p*-type materials. The *p*- and *n*-legs were connected electrically in series and thermally in parallel by the copper interconnect high-temperature brazing material.

Device measurement

The contact resistance of legs was measured using home-made scanning probe system [48]. The simultaneous measurement of the output power and the efficiency for TEG was performed under the vacuum condition with a pressure of $\sim 10^{-6}$ mbar. A constant heat flow from the heater was applied on top side of TEG using home-made power supply. The TEG output performance was evaluated by recording the open circuit voltage (V_{oc}), device voltage (V_d), internal resistance (r_i) and the peak power output (P_{max}) with changing hot side temperature from 473 K to 1023 K under constant cold-side temperature at 293 K. The detailed set up of the measurement is illustrated in the [Supplementary Fig. S5](#).

Data availability

The data that support the plots within this paper and other findings of this study are available from the corresponding author upon reasonable request.

Acknowledgements

The authors are thankful to Dr. Hsin Wang, Oakridge National Laboratory, for validation of thermoelectric properties and Christopher Winkler for assistance with analysis of HRTEM data. HBK, BP, WL, US and HL acknowledge financial support from DARPA Nano Engineered Thermoelectric Systems (NETS) program (HR0011-16-C-0035). SP acknowledges the support from National Science Foundation program through I/UCRC: Center for Energy Harvesting Materials and Systems (CEHMS). MGK acknowledges the support from Air Force office of Scientific Research under award number: FA9550-17-1-0341.

Competing financial interests

The authors declare no competing financial interest.

Appendix A. Supplementary data

Supplementary data to this article can be found online at <https://doi.org/10.1016/j.mattod.2020.01.002>.

References

- [1] B.L. Blaney, Industrial Waste Heat Recovery and the Potential for Emissions Reduction, US Environmental Protection Agency, Industrial Environmental Research Laboratory, 1984.
- [2] J.L. Pellegrino et al., Energy Use, Loss and Opportunities Analysis: US Manufacturing & Mining, US Department of Energy, Energetics, and E3M, 2004.
- [3] V.V. Viswanathan et al., Opportunity Analysis for Recovering Energy from Industrial Waste Heat and Emissions, Pacific Northwest National Laboratory (PNNL), 2006.
- [4] I. Johnson et al., Waste Heat Recovery. Technology and Opportunities in US Industry, BCS, Inc., Laurel, MD (United States), 2008.
- [5] C. Forman et al., *Renew. Sust. Energ. Rev.* 57 (2016) 1568.
- [6] S. Chen, Z.F. Ren, *Mater. Today* 16 (10) (2013) 387.
- [7] R. He et al., *Phys. Status Solidi A* 212 (10) (2015) 2191.
- [8] G. Rogl et al., *Acta Mater.* 107 (2016) 178.
- [9] I. Galanakis et al., *Phys. Rev. B* 66 (13) (2002) 134428.
- [10] J. Yang et al., *Adv. Funct. Mater.* 18 (19) (2008) 2880.
- [11] C. Uher et al., *Phys. Rev. B* 59 (13) (1999) 8615.
- [12] H. Xie et al., *Sci. Rep.* 4 (2014) 6888.
- [13] X. Yan et al., *Energy Environ. Sci.* 5 (6) (2012) 7543.
- [14] J. Yang et al., *Appl. Phys. Lett.* 85 (7) (2004) 1140.
- [15] S. Bhattacharya et al., *Phys. Rev. B* 77 (18) (2008) 184203.
- [16] S. Bhattacharya et al., *Appl. Phys. Lett.* 81 (1) (2002) 43.
- [17] G. Joshi et al., *Adv. Energy Mater.* 1 (4) (2011) 643.
- [18] X.A. Yan et al., *Nano Lett.* 11 (2) (2011) 556.
- [19] S.V. Faleev, F. Léonard, *Phys. Rev. B* 77 (21) (2008) 214304.
- [20] M. Zebarjadi et al., *Appl. Phys. Lett.* 94 (20) (2009) 202105.
- [21] M. Zebarjadi et al., *J. Electron. Mater.* 38 (7) (2009) 954.
- [22] J.P. Heremans et al., *J. Appl. Phys.* 98 (6) (2005) 063703.
- [23] S. Sumithra et al., *Adv. Energy Mater.* 1 (6) (2011) 1141.
- [24] J.P.A. Makongo et al., *J. Am. Chem. Soc.* 133 (46) (2011) 18843.
- [25] P. Sahoo et al., *J. Mater. Chem. A* 2 (24) (2014) 9298.
- [26] W.J. Xie et al., *Acta Mater.* 58 (14) (2010) 4705.
- [27] W.J. Xie et al., *Acta Mater.* 61 (6) (2013) 2087.
- [28] K.S. Kim et al., *Adv. Mater.* 29 (36) (2017) 170209.
- [29] Y.T. Liu et al., *Adv. Mater.* 30 (32) (2018) 1800881.
- [30] H. Zhao et al., *Adv. Energy Mater.* 7 (18) (2017) 1700446.
- [31] S. Chen et al., *Adv. Energy Mater.* 3 (9) (2013) 1210.
- [32] C.C. Hsu et al., *J. Alloy. Compd.* 597 (2014) 217.
- [33] M. Schwall, B. Balke, *Phys. Chem. Chem. Phys.* 15 (6) (2013) 1868.
- [34] C. Yu et al., *J. Mater. Res.* 27 (19) (2012) 2457.
- [35] A. Visconti et al., *Scr. Mater.* 123 (2016) 100.
- [36] K. Biswas et al., *Nature* 489 (7416) (2012) 414.
- [37] M.X. Zhang, P.M. Kelly, *Scr. Mater.* 52 (10) (2005) 963.
- [38] M. Cutler, N.F. Mott, *Phys. Rev.* 181 (3) (1969) 1336.
- [39] J.P. Heremans et al., *Science* 321 (5888) (2008) 554.
- [40] H.-S. Kim et al., *APL Mater.* 3 (4) (2015) 041506.
- [41] Y. Liu et al., *APL Mater.* 4 (10) (2016) 104813.
- [42] H. Muta et al., *Mater. Trans.* 47 (6) (2006) 1453.
- [43] J. Zhang et al., *Adv. Mater.* 29 (39) (2017) 1703148.
- [44] H. Lee et al., *Appl. Energy* 211 (2018) 987.
- [45] X. Ka et al., *J. Phys. D* 43 (11) (2010) 115303.
- [46] W. Liu et al., *J. Mater. Chem. A* 1 (42) (2013) 13093.
- [47] H.T. Zhu et al., *Nat. Commun.* 9 (2018) 9.
- [48] G. Joshi, B. Poudel, *J. Electron. Mater.* 45 (12) (2016) 6047.
- [49] T.J. Zhu et al., *Adv. Energy Mater.* 5 (19) (2015) 1500588.
- [50] Y. Zhang et al., *Energ. Convers. Manage.* 105 (2015) 946.
- [51] K. Bartholome et al., *J. Electron. Mater.* 43 (6) (2014) 1775.
- [52] R. Hea et al., *PNAS* 113 (48) (2016) 13576.